

Kagome edge states under lattice termination, spin-orbit coupling, and magnetic order

Sajid Sekh,^{1,*} Annica M. Black-Schaffer,² and Andrzej Ptak^{1,†}

¹*Institute of Nuclear Physics, Polish Academy of Sciences, W. E. Radzikowskiego 152, PL-31342 Kraków, Poland*

²*Department of Physics and Astronomy, Uppsala University, Box 516, S-751 20 Uppsala, Sweden*

(Dated: February 13, 2026)

We study the edge state properties of a two-dimensional kagome lattice using a tight-binding approach, focusing on the role of lattice termination, spin-orbit coupling, and magnetic order. In the pristine limit, we show that the existence of localized edge states is highly sensitive to boundary geometry, with certain terminations completely suppressing edge modes. Kane-Mele spin-orbit coupling opens a bulk gap and stabilizes topologically protected helical edge states, yielding a robust \mathbb{Z}_2 insulating phase that is insensitive to termination details. In contrast, the combined effect of a Zeeman field and Rashba spin-orbit coupling drives the system into Chern insulating phases, with Chern numbers consistent with the number of chiral edge modes. We further demonstrate that non-coplanar magnetic textures generate multiple Chern phases through finite scalar spin chirality, with Kane-Mele coupling strongly tuning the topological gaps. Our results provide important insights into the tunability of edge states in the kagome lattice, which can be key to designing materials with novel electronic properties and topological phases.

I. INTRODUCTION

Edge states refer to low-dimensional electronic states that are pinned to the boundaries of a material. They play a central role in topological condensed matter. In fact, the bulk-boundary correspondence [1], a foundational principle in topological physics, dictates that non-trivial bulk invariants manifest as gapless modes confined to system boundaries. Edge states can thus serve both as a signature of nontrivial bulk topology and as functional channels for robust, dissipation-resistant transport.

At the same time, two-dimensional (2D) kagome lattice has emerged as a particularly rich platform for exploring novel phenomena. The structure of the kagome lattice is formed by corner-sharing triangles arranged in a hexagonal fashion, which provides geometrical frustration, preventing spins from aligning magnetically. This leads to exotic kagome spin ice states [2, 3], emergent gauge fields [4], and fractionalized excitations [5, 6]. Apart from spins, the kagome lattice is also exciting from an electronic perspective as the band structure contains Dirac cones, van Hove singularities (VHS), and flat bands (FB) at various fillings. The existence of a large density of states around VHS and FB can produce strong correlation effects. These features underpin a variety of exotic phases such as charge [7–9], spin [10], and pair density waves [11], nematicity [12–15], skyrmionic texture [16, 17], loop currents [18], and unconventional superconductivity [19–21] in kagome materials.

Edge states are an exciting avenue for unlocking the potential of the kagome lattice. In a pristine lattice system, the properties of edge states often strongly depend on the details of the boundary, making lattice ter-

mination a crucial factor. This dependence is already well-known in the honeycomb lattice of graphene [22–25], where the nature of the edge dramatically influences the electronic spectrum: zigzag termination supports localized, nearly flat edge states at half filling, which give rise to enhanced local density of states and magnetism, whereas armchair termination lacks such modes. The sensitivity to termination has also been shown to be crucial for building quantum devices [26–28], and we can expect an even richer scenario in kagome lattices due to their corner-sharing triangular geometry. In fact, experimentally, lattice termination has already emerged as a viable tool to design and manipulate edge states in kagome materials. For instance, in the magnetic kagome material $\text{Co}_3\text{Sn}_2\text{S}_2$ [29], different termination planes produce contrasting surface states near the Fermi level. Similarly, a “terrace”-like geometry in antiferromagnetic FeGe [30, 31], where kagome layers form a staircase pattern with distinct edge boundaries at each step, has revealed spin-polarized edge states around the Fermi level, further enhanced by charge order. Although some effort [32] has been made to understand the pristine case, it is not exhaustive, and in particular, does not answer how the edge states intertwine with spin-orbit coupling (SOC) and magnetism.

In fact, kagome materials are known to possess finite SOC, which can substantially enhance Berry curvature to produce nontrivial edge states. The role of SOC in generating topological phases is elucidated in the Kane-Mele model [33], where spin-dependent next-nearest-neighbor hopping and a staggered potential give rise to a \mathbb{Z}_2 topological insulating phase in the honeycomb lattice. Although formulated as a toy model, the underlying mechanism extends to kagome lattices. For example, first-principle analysis of the nonmagnetic kagome material KV_3Sb_5 [20] has revealed a \mathbb{Z}_2 topological phase in the normal state, where the \mathbb{Z}_2 nature is confirmed by the wavefunction parity at time-reversal invariant momenta.

* e-mail: sajid.sekh@ifj.edu.pl

† e-mail: aptok@mmj.pl

The \mathbb{Z}_2 phase remains intact as long as the time-reversal symmetry (TRS) is present.

An external magnetic field is well-known to break TRS. More interestingly, TRS can also be broken by intrinsic magnetism or chiral charge order. The breaking of TRS can induce a topological Chern phase, characterized by a nonzero Chern number, which underlies the quantum anomalous Hall (QAH) effect. In the QAH state, a transverse Hall current arises purely from the Berry curvature of the electronic bands, without the need for an applied magnetic field. In magnetic kagome systems, the QAH phase has so far been found to be driven by ferromagnetism, with experimental signatures, including anomalous transport and neutron diffraction, having confirmed ferromagnetic order in Fe- and Co-based kagome compounds [34–36], as well as in the kagome-based 166 family [37]. In addition, scanning microscopy results of an Fe-based kagome compound [30] have revealed pronounced edge states within the bulk gap. The ferromagnetism can be effectively modeled as an out-of-plane Zeeman field. Such a Zeeman field produces spin-split bands, analogous to the scenario in 1D Majorana nanowires [38], which have been proposed [39] as a platform for fault-tolerant [40] quantum computation.

The QAH can also be realized with more complex magnetic orders beyond ferromagnetism. Unlike simple ferromagnets or antiferromagnets, spins on the kagome lattice often form noncollinear arrangements, with the planar 120° “ $\mathbf{q} = 0$ ” configuration [41–44] being the simplest example. While this coplanar order does not break TRS, a non-coplanar canting of the spins has been shown to generate a finite scalar spin chirality, which can induce a QAH [45] phase. Such canting can arise naturally from Dzyaloshinskii–Moriya interactions [46] or at interfaces in thin films, producing an “umbrella”-like spin structure. This non-coplanar order opens a topological bulk gap, but although the QAH phase has been predicted [45], the edge state dispersion and interplay with spin-orbit coupling remain largely unexplored for such magnetic configurations. Understanding these will allow us to have more precise and tunable control of non-trivial edge states in a realistic setup.

Motivated by the extensive work on kagome materials, we perform a systematic study to advance the understanding of edge states in the kagome lattice. In particular, we analyze, using a tight-binding approach, how different lattice terminations shape both the edge state spectrum and local density of states (LDOS), providing a direct link to experimental spectroscopic signatures. Beyond lattice termination, we show that SOC and magnetic order play a crucial role in determining the topological origin and spin polarization of edge states. Although previous studies have explored [32, 44, 47–49] SOC in kagome systems, a detailed investigation of the interplay between edge termination, SOC, and magnetic order remains lacking. Here, we address this gap by considering both intrinsic and extrinsic SOC, as well as ferromagnetic and antiferromagnetic orders, to reveal their distinct ef-

fects on the edge state structure.

We organize the work as follows. We begin by discussing the bulk features of the kagome lattice in Sec. II. We show the slab band structure and LDOS to show the effects of lattice termination in Sec. III. We present results including Kane–Mele SOC in Sec. IV, followed by a discussion of effective Zeeman field and Rashba SOC in Sec. V. We consider the non-coplanar magnetic texture in Sec VI. Finally, we conclude our work in Sec. VII.

II. KEY PROPERTIES OF THE KAGOME BAND STRUCTURE

We start with a single orbital tight-binding description of the kagome lattice [see Fig. 1(a)]

$$H_{\text{KIN}} = -t \sum_{\langle ij \rangle \sigma} c_{i\sigma}^\dagger c_{j\sigma} - \mu \sum_{i\sigma} c_{i\sigma}^\dagger c_{i\sigma}, \quad (1)$$

where $c_{i\sigma}^\dagger$ ($c_{i\sigma}$) creates (annihilates) an electron with spin σ at the i -th lattice site. The notation $\langle \dots \rangle$ indicates hopping is restricted to the nearest neighbor (NN), t is the amplitude of the NN hopping integral, and μ is the chemical potential. To obtain the band structure, we perform a Fourier transformation and write the Hamiltonian in momentum space

$$\mathcal{H}_{\text{KIN}} = \sum_{\mathbf{k}\sigma} \psi_{\mathbf{k}\sigma}^\dagger h_{\text{KIN}}(\mathbf{k}) \psi_{\mathbf{k}\sigma}. \quad (2)$$

Here the basis is given by $\psi_{\mathbf{k}\sigma} = [c_{\mathbf{k}A\sigma}, c_{\mathbf{k}B\sigma}, c_{\mathbf{k}C\sigma}]^T$, where $c_{\mathbf{ks}\sigma}$ is an annihilation operator of electron with spin σ and momentum \mathbf{k} in sublattice $s \in \{A, B, C\}$. The kernel of the Hamiltonian reads

$$h_{\text{KIN}}(\mathbf{k}) = \begin{bmatrix} -\mu & -2t \cos \delta_1 & -2t \cos \delta_3 \\ -2t \cos \delta_1 & -\mu & -2t \cos \delta_2 \\ -2t \cos \delta_3 & -2t \cos \delta_2 & -\mu \end{bmatrix}. \quad (3)$$

For brevity, we use the notation $\delta_i = \mathbf{k} \cdot \mathbf{d}_i$, where $\mathbf{k} = (k_x, k_y)$ is the 2D wavevector, and $\mathbf{d} \in \{\mathbf{a}_1/2, \mathbf{a}_2/2, (\mathbf{a}_1 - \mathbf{a}_2)/2\}$ is the vector connecting NN sites [see Fig. 1(a)]. The eigenvalues of Eq. (3) are given by $E(\mathbf{k}) = 2t, -t[1 \pm \sqrt{f(\mathbf{k})}]$ with $f(\mathbf{k}) = [3 + 2 \cos k_x + 4 \cos(k_x/2) \cos(\sqrt{3}k_y/2)]$, for μ set to zero. We plot the band structure along the high symmetry path in Fig. 1(b), which shows two dispersive and one flat band (FB). Notably, the dispersive bands contain a Dirac point (DP) at K (K') and saddle points at M, which leads to a logarithmic van Hove singularity (VHS) in the density of states (DOS) [see right panel in Fig. 1(b)].

III. CRYSTALLINE EDGE STATES: TERMINATION DEPENDENCE

We begin by examining the edge states of the pristine kagome lattice described by Eq. (1). Edge states

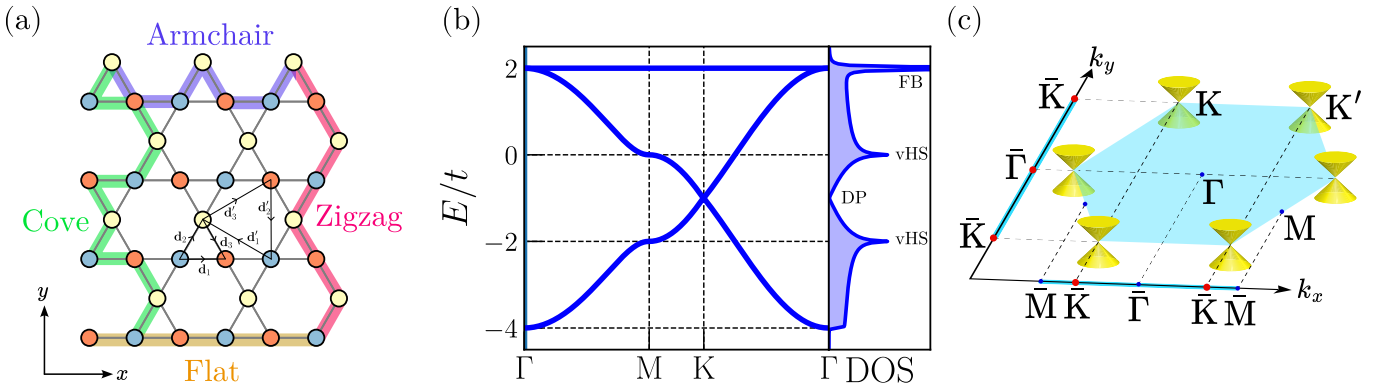


FIG. 1. (a) Kagome lattice, schematically highlighting the four edge types arising from termination by a line cut. Solid arrows indicate nearest $\mathbf{d}_{1,2,3}$ and next-nearest $\mathbf{d}'_{1,2,3}$ neighbor vectors, while site color-coding refers to the three sublattice atoms of the kagome lattice. (b) Band structure (left) and density of states (DOS) (right) in the kagome lattice, with features of Dirac point (DP), van Hove singularity (VHS), and flat band (FB) appearing at different fillings. (c) Full (blue hexagon) and projected slab (blue line) Brillouin zones of the kagome lattice. In contrast to the full Brillouin zone, the high symmetry points in the slab are written with bar. Yellow cones denote the Dirac points.

are important because they can substantially alter the electronic properties of a system, and provide direct insight into bulk topology. Since edge states cannot exist in an infinite lattice without boundaries, their study requires an explicit lattice termination. This prompts us to consider a “slab geometry” to study the edge states of kagome lattice. A 2D slab structure implies that one of the directions is under periodic boundary conditions, while the other direction is finite. For simplicity, we restrict ourselves to line cuts along the main axes in this work. This leads to four types of edge patterns on the kagome lattice: zigzag, armchair, cove, and flat [see Fig. 1(a)]. To showcase the periodicity of the slab, we present the Brillouin zone (BZ) in Fig. 1(c). The hexagon represents the bulk BZ, where the Dirac points are symmetrically located at the corners. A slab with edges at fixed x has periodic BZ along k_y direction — this leads to the high symmetry path: $\bar{K}-\bar{\Gamma}-\bar{K}$. Similar arguments can be used for other directions.

To analyze the edge states, we focus on the slab band structure obtained from exact diagonalization of Eq. (1). We are also interested in how the edge states are distributed in the real-space lattice, and for this, we examine the local density of states (LDOS). Since the edge state does not always lie inside a fully gapped spectrum, we use the momentum-resolved site LDOS:

$$\rho_i(E, k_a) = \sum_n |\psi_{in}(k_a)|^2 \delta[E - E_n(k_a)], \quad (4)$$

Here, ψ_{in} is the wavefunction of the n -th state with energy $E_n(k_a)$, $a = x, y$ labels the axis, and i denotes the lattice sites. We approximate the delta function by a Lorentzian $\delta(x) = (\epsilon/\pi)/(x^2 + \epsilon^2)$, with a small broadening $\epsilon = 10^{-3}$. For illustrative purposes, we usually pick the energy E to correspond to an edge state at momentum k_a that maximizes the number of edge states relative to bulk states.

A. Edge types at fixed y

First, we describe three possible terminations at fixed y axis: armchair or flat terminations for both slab edges or one for each edge. The armchair termination hosts two edge states in the band structure [see Fig. 2(a)]: one that connects the DPs from \bar{K} and \bar{K}' , while the other exists near the FB, see triangle and star icons, respectively. For further analysis, we pick the \bar{M} point (red vertical line), and plot the energy levels against the state index, next to the band structure. The spectrum shows three continuous spectra arising from the bulk bands, plus two pairs of isolated states located in the gaps. These gapped states lie at opposite energies and are two-fold degenerate. Here, the degeneracy stems from the similarity between the top and bottom edges. It is worthwhile to mention that, even with similar edge types, mirror symmetry may not always be present. This is the case when opposite edges are connected by screw symmetry (reflection+translation), even though they are of the same type. Nonetheless, we find no difference in the band structure in the presence and absence of mirror symmetry (results not shown). Also plotting the edge state LDOS at the \bar{M} point, we find that the electrons are mostly localized at the boundaries. More specifically, the LDOS strongly peaks at the edge sites with two nearest neighbors. We notice that the LDOS map forms a triangular plaquette at the edge. Electrons (of s -type) moving in such cycloid trajectory are predicted to carry a finite orbital angular momentum (OAM) [50]. Inside the bulk, neighboring upward and downward triangles negate the OAM, but this cancellation does not occur at the edges. The OAM arises due to translation and rotation and thus a finite group velocity $v_{\mathbf{k}} = \partial_{\mathbf{k}} E(\mathbf{k})$ of kagome edge states can be useful in orbitronics.

For the flat edge termination, we find that the edge

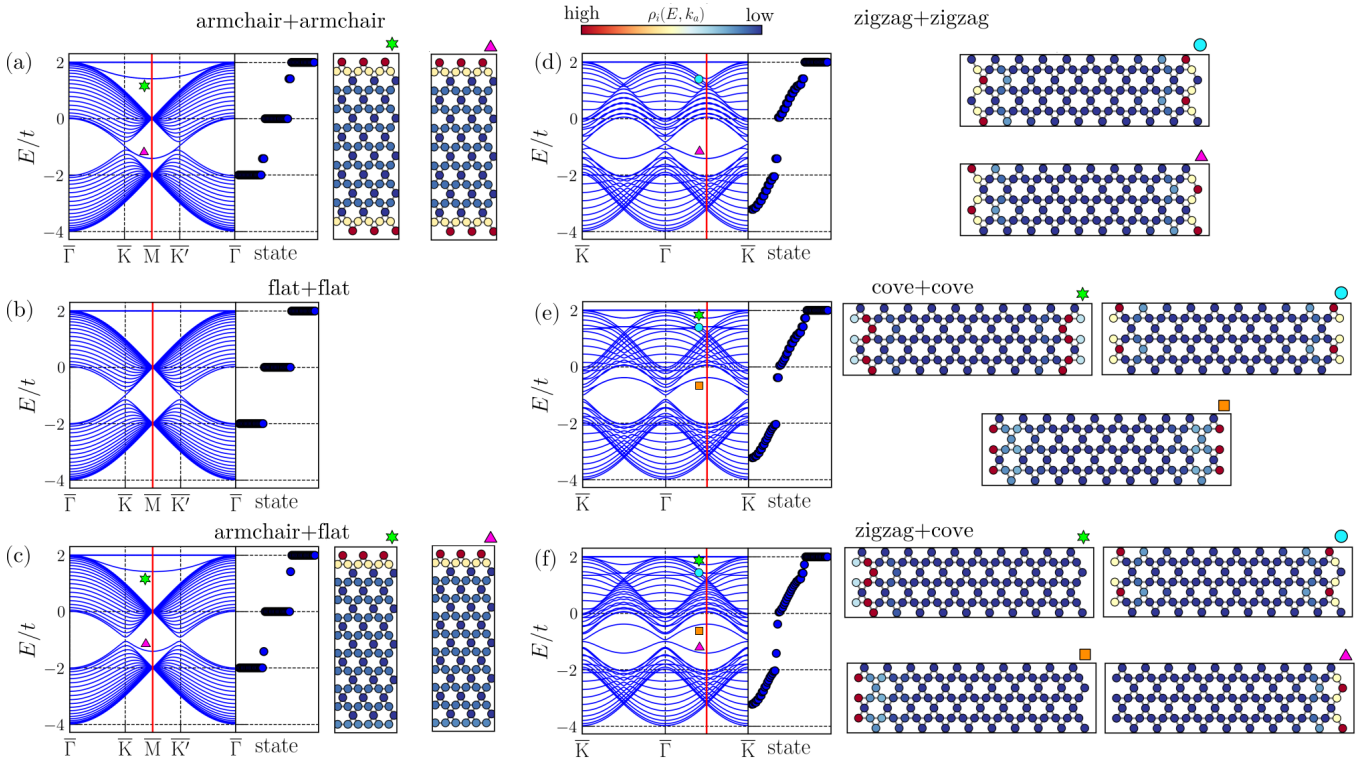


FIG. 2. Kagome slab band structure for different lattice terminations (left), with energy levels at a specific momentum (red vertical line) to pinpoint the edge states (middle), edge states are highlighted by icons, and we present the momentum-resolved site LDOS on real-space lattice (right). Parameters are $\mu/t = 0$ and $t = 1$.

states completely disappear [see Fig. 2(b)]. This type of termination instead yields a band structure similar to the bulk, with no in-gap edge states. For this reason, we omit the LDOS. Finally, we turn to the case where one side of the slab has armchair-termination, and the other flat termination [see Fig. 2(c)]. We find that the resulting edge states are similar to the armchair termination. However, in contrast, the edge states are no longer two-fold degenerate due to the lack of mirror symmetry. The LDOS shows that both edge states are localized at the armchair termination, as expected from the results in Fig. 2(a,b).

B. Edge types at fixed x

We next focus on edge terminations at fixed x axis, which are zigzag, cove, and a mix of both. We begin by analyzing the band structure of the pure zigzag termination [see Fig. 2(d)]. The bulk spectrum contains three DPs at the \bar{K} , \bar{K}' , and $\bar{\Gamma}$, respectively. Interestingly, the DP at the $\bar{\Gamma}$ point appears due to projection of the K point onto the Γ point [see Fig. 1(c)]. This is in contrast to the slab BZ along the k_x direction, which has only two DPs. Therefore, specific lattice terminations can dictate hybridization at the Γ point with other states (e.g. substrate/impurity), which is important for device ap-

plications. In the energy spectrum, there exist two edge states – one connecting the DPs (triangle) and another near the FB (circle), reminiscent of the armchair case. For our analysis, we here take an energy cut (highlighted by red line) between the $\bar{\Gamma}$ and \bar{K} points, and plot the LDOS. We see that the in-gap states are localized at the slab boundary as edge states. Due to mirror symmetry, the edge states are degenerate. Depending on the edge state energy, the LDOS acquires a phase shift so that the maximum LDOS is on a site with either two or four NN sites.

As we move to the cove termination [see Fig. 2(e)], non-degenerate edge states appear in the spectrum. Specifically, the edge state marked by the circle is twofold degenerate, while others are now non-degenerate states. The LDOS shows that all edge states are localized, but with some spread into the bulk. Here, only the edge state close to zero energy localizes on a dangling site; other edge states are localized on non-dangling edge sites with four NN sites, further into the slab.

Finally, we consider a mix of zigzag and cove terminations [see Fig. 2(f)]. We find that mixing both terminations yields all possible edge states from each type of termination. We thus find five edge states, but one of the edge states (marked by a circle) is two-fold degenerate. According to the LDOS, only the degenerate state has edge states on both sides of the slab. For all the other

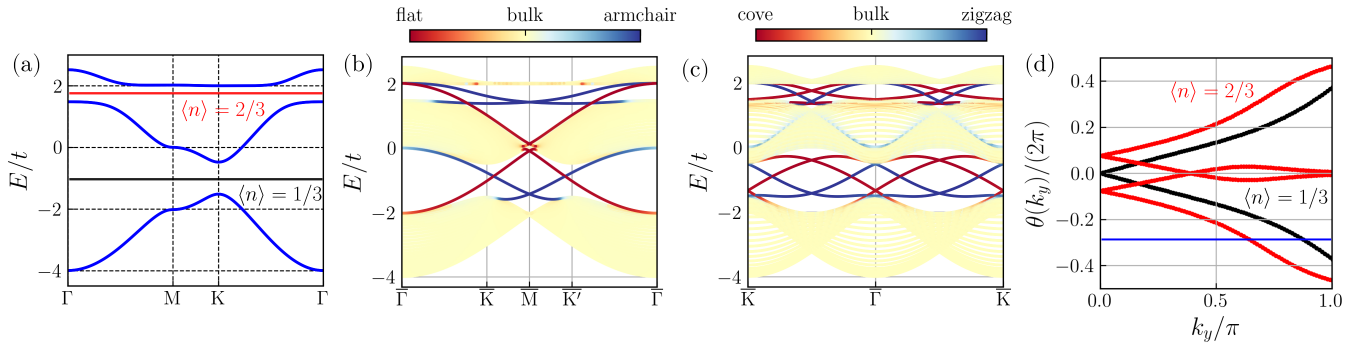


FIG. 3. (a) Bulk kagome bands for the QSH phase and the slab band structure for (b) armchair-flat and (c) zigzag-cove type terminations. In all bandstructure plots, we take $\lambda_{\text{KM}}/t = 0.15$ and $\mu/t = 0$. Colors show expectation of the position operator. (d) Eigenvalues of the Wilson loop plotted as a function of k_y for two different fillings, as indicated in (a). Eigenvalues of both fillings $\langle n \rangle$ cross the reference line (blue line) once (odd number of times), indicating the \mathbb{Z}_2 nature.

cases, the edge state localizes on the cove termination, as expected. Overall, we find that the pristine kagome lattice hosts a multitude of edge states, strongly dependent on the lattice terminations.

IV. QUANTUM SPIN HALL PHASE AND \mathbb{Z}_2 CLASSIFICATION

Kagome materials are known to exhibit intrinsic SOC. It was first reported in the ferromagnetic nodal-line semimetal Fe_3Sn_2 [48, 51], where SOC fully gaps out the nodal lines, leading to massive Dirac bands. Later, intrinsic SOC was also confirmed in 135 [19] and 166 [52] kagome materials. In this section, we investigate how the crystalline edge states change under intrinsic SOC. More specifically, we choose Kane–Mele type SOC (KMSOC), which is a prototypical model for the quantum spin Hall (QSH) effect. The SOC Hamiltonian can be written as

$$H_{\text{QSH}} = H_{\text{KIN}} + H_{\text{KM}}, \quad (5)$$

Here, the first term refers to the kinetic part described in Eq. (1), while the latter term denotes the KM part

$$H_{\text{KM}} = i\lambda_{\text{KM}} \sum_{\langle\langle ij \rangle\rangle\sigma} \nu_{ij} c_{i\sigma}^\dagger \sigma_z c_{j\sigma}, \quad (6)$$

where λ_{KM} is the strength of the coupling and σ_z is the third Pauli matrix acting in spin subspace. The notation $\langle\langle \dots \rangle\rangle$ means KMSOC is a NNN hopping with a chiral factor ν , which takes values 1 or -1 if the hopping is anticlockwise or clockwise, respectively. Note that H_{KM} preserves time-reversal symmetry (TRS) since opposite spins are assigned opposite chiralities.

First, we look at the bulk bands to get insight into the KM term. In the momentum space, we write the KM Hamiltonian in the three-sublattice (A, B, C) kagome spinful (\uparrow, \downarrow) basis $\psi_{\mathbf{k}} =$

$$[c_{\mathbf{k}A\uparrow}, c_{\mathbf{k}B\uparrow}, c_{\mathbf{k}C\uparrow}, c_{\mathbf{k}A\downarrow}, c_{\mathbf{k}B\downarrow}, c_{\mathbf{k}C\downarrow}]^T$$

$$h_{\text{KM}}(\mathbf{k}) = \sigma_z \otimes 2i\lambda_{\text{KM}} \begin{bmatrix} 0 & \cos \tau_3 & -\cos \tau_1 \\ -\cos \tau_3 & 0 & \cos \tau_2 \\ \cos \tau_1 & -\cos \tau_2 & 0 \end{bmatrix}, \quad (7)$$

where $\tau_i = \mathbf{k} \cdot \mathbf{d}'_i$, \mathbf{k} is the wavevector, and \mathbf{d}'_i are the vectors connecting NNN sites. The bulk bands are presented in Fig. 3(a). We find that a finite KM coupling $\lambda_{\text{KM}}/t = 0.15$ opens band gaps at two locations: one at \mathbf{K} and the other one near FB. The presence of KMSOC also makes the FB dispersive.

The opening of band gap leads to gapless edge states in a slab geometry [see Fig. 3(b,c)]. Here, we consider two types of slabs with mixed edges, and keep the slab width large enough to avoid any hybridization between edge states. It is also judicious to project the expectation of the position operator on the bands to pinpoint edge state localization [53]. For this, we introduce the position-weighted amplitude

$$\rho_{n,a}(\mathbf{k}) = \sum_i |\psi_{in}(\mathbf{k})|^2 \mathbf{r} \cdot \hat{e}_a, \quad (8)$$

where \mathbf{r} is the position operator, ψ_{in} is the wavefunction of the n -th state, and \hat{e}_a is the unit vector along length $a = x, y$. For both slab directions, we find that each boundary contains two localized edge states in each gap [see Fig. 3(b,c)]. What is interesting is that the SOC enables the flat boundary to host edge states, even though it does not exhibit any edge states without KMSOC. For the zigzag-cove edge type, we also notice that bands at $\bar{\Gamma}$ and \bar{K} are similar – this happens due to projection of the DP on $\bar{\Gamma}$ as shown in Fig. 1(c). We can verify the presence of TRS since $E(\bar{K}) = E(\bar{K}')$.

To classify the topology of the TRS bands, we compute the \mathbb{Z}_2 index, which is the topological invariant for QSH [33, 54] phase. A time-reversal invariant QSH phase has $\mathbb{Z}_2 = 1$, which distinguishes it from ordinary insulators with $\mathbb{Z}_2 = 0$. One of the ways to compute the

\mathbb{Z}_2 index is through the Wilson loop formalism [55, 56]. This method is equivalent to tracking maximally localized Wannier centers [57, 58]. In this approach, we define the transfer matrix in the discretized BZ

$$W(k_y) = \prod_i \mathbf{P}_{i,i+1}(k_y), \quad (9)$$

where $P_{i,i+1}^{mn}(k_y) = \langle u_m(k_x^i, k_y) | u_n(k_x^{i+1}, k_y) \rangle$ is the overlap matrix, (m, n) refer to occupied bands, and $|u_n\rangle$ is the Bloch wavefunction. Given N_{occ} occupied bands, $W(k_y)$ is a $N_{\text{occ}} \times N_{\text{occ}}$ matrix with eigenvalues $\lambda_1, \lambda_2, \dots, \lambda_{N_{\text{occ}}}$. Then the phase of the eigenvalues is

$$\theta_n(k_y) = \text{Im}[\ln \lambda_n(k_y)]. \quad (10)$$

The winding of the phase factor $\theta(k_y)$ for each eigenvalue against k_y is key to infer the \mathbb{Z}_2 index. More specifically, if $\theta(k_y)$ crosses a reference line θ_c odd number of times, we have $\mathbb{Z}_2 = 1$, otherwise it is trivial and $\mathbb{Z}_2 = 0$.

We show the evolution of $\theta(k_y)$ in Fig. 3(d) at two different fillings. We recall that the number of eigenvalues is determined by the number of occupied bands. Owing to spin degeneracy, there are two occupied bands at 1/3 filling and four at 2/3 filling, which accounts for the corresponding number of solutions at each filling. Due to TRS, k_y is evolved through half of BZ; in fact, $k_y = 0$ and $k_y = 2\pi$ are Kramers-degenerate points related by TRS. As k_y is varied from 0 to π , we observe that $\theta(k_y)$ exhibits an approximately π jump for both fillings. Importantly, upon choosing a reference line $\theta_c = -0.3$, $\theta(k_y)$ crosses this line once (or, more generally, an odd number of times), signaling non-trivial \mathbb{Z}_2 bulk topology.

A direct consequence of the \mathbb{Z}_2 phase is the presence of helical edge states, namely, pairs of spin-polarized edge modes that propagate in opposite directions. This is thus the origin of edge states in Fig. 3(b,c) in both bulk gaps, where the edge states associated with a given boundary exhibit opposite slopes, indicating counter-propagating motion. Furthermore, these counter-propagating modes carry opposite spin polarizations, as confirmed by the spin-polarized band structure in Fig. SF1 in the Supplemental Material (SM) [59]. Thus, the inclusion of KM-SOC gaps out the otherwise gapless edge modes of the pristine kagome lattice, yielding helical, spin-polarized edge states that are consistent with a \mathbb{Z}_2 topological phase. The resulting edge dispersion respects the \mathbb{Z}_2 symmetry, such that the edge modes appear in Kramers pairs, are spin-polarized, and their number is independent of the lattice termination.

V. QUANTUM ANOMALOUS HALL PHASE VIA FERROMAGNETISM

A. Zeeman field and Rashba SOC

The QSH phase discussed in Sec. IV evolves into a QAH phase once TRS is broken [60]. The key signature

of this phase is an anomalous Hall conductivity, which is a Hall response generated without any magnetic field [61]. Motivated by the occurrence of ferromagnetism (FM) in kagome materials [34, 36, 62], we use a Zeeman field to provide a simple mechanism to break TRS. In fact, the kagome lattice generally supports FM due to the presence of a non-dispersive FB [63] or a VHS [64], if appearing near the Fermi level. In magnetic kagome semimetals, the inclusion of SOC lifts the nodal line degeneracies [65, 66], which can be modeled by RSOC [67].

The anomalous Hall conductivity is known to be quantized [68–70] in units of e^2/h inside a global topological gap. This is called a Chern insulating phase, which is characterized by a \mathbb{Z} invariant known as the Chern number. To achieve a quantized QAH, pairing the Zeeman, or exchange, field with Rashba SOC (RSOC) is often useful. While the exchange field creates spin-polarized bands, the RSOC can further lift spin degeneracy in momentum space to create a bulk gap [71, 72]. The RSOC leads to so-called “spin-momentum locking” – a phenomenon where spin orientation depends on momentum, and as a result, the bulk bands exhibit a momentum-dependent splitting. An important distinction is that, unlike KM-SOC, the RSOC mixes the spin sector, so that S_z is no longer a conserved quantum number. The appearance of a Rashba term requires broken inversion symmetry, which in practice can arise due to non-centrosymmetric stacking of layers or surface/interface effects.

We add FM and RSOC in the kagome lattice through the following minimal Hamiltonian

$$H_{\text{QAH}} = H_{\text{KIN}} + H_R + H_Z, \quad (11)$$

where the first term is introduced in Eq. (1). The second and third terms describe the Hamiltonian for RSOC and out-of-plane Zeeman field, respectively

$$H_R = -i\lambda_R \sum_{\langle ij \rangle, \sigma\sigma'} c_{i\sigma}^\dagger (\mathbf{d}_{ij} \times \boldsymbol{\sigma}_{\sigma\sigma'})_z c_{j\sigma'}, \quad (12)$$

$$H_Z = -h_z \sum_i (c_{i\uparrow}^\dagger c_{i\uparrow} - c_{i\downarrow}^\dagger c_{i\downarrow}). \quad (13)$$

In the RSOC Hamiltonian, λ_R denotes the strength of the spin-orbit coupling. The Zeeman field creates a splitting of h_z between opposite spins at the i -th site.

In momentum space, we express the Hamiltonian in the same basis as h_{KM} in Eq. (7):

$$h_R(\mathbf{k}) = \sigma_y \otimes \lambda_R \begin{bmatrix} 0 & \sin \delta_1 & \gamma^* \sin \delta_3 \\ \sin \delta_1 & 0 & \gamma \sin \delta_2 \\ \gamma^* \sin \delta_3 & \gamma \sin \delta_2 & 0 \end{bmatrix},$$

$$h_Z(\mathbf{k}) = \sigma_z \otimes \begin{bmatrix} h_z & 0 & 0 \\ 0 & h_z & 0 \\ 0 & 0 & h_z \end{bmatrix}, \quad (14)$$

where we denote $\delta_i = \mathbf{k} \cdot \mathbf{d}_i$ and $\gamma = i \exp(i\pi/6)$. We illustrate the bulk band structure in Fig. 4(a). The Zeeman field leads to spin-polarized and -split bands, which

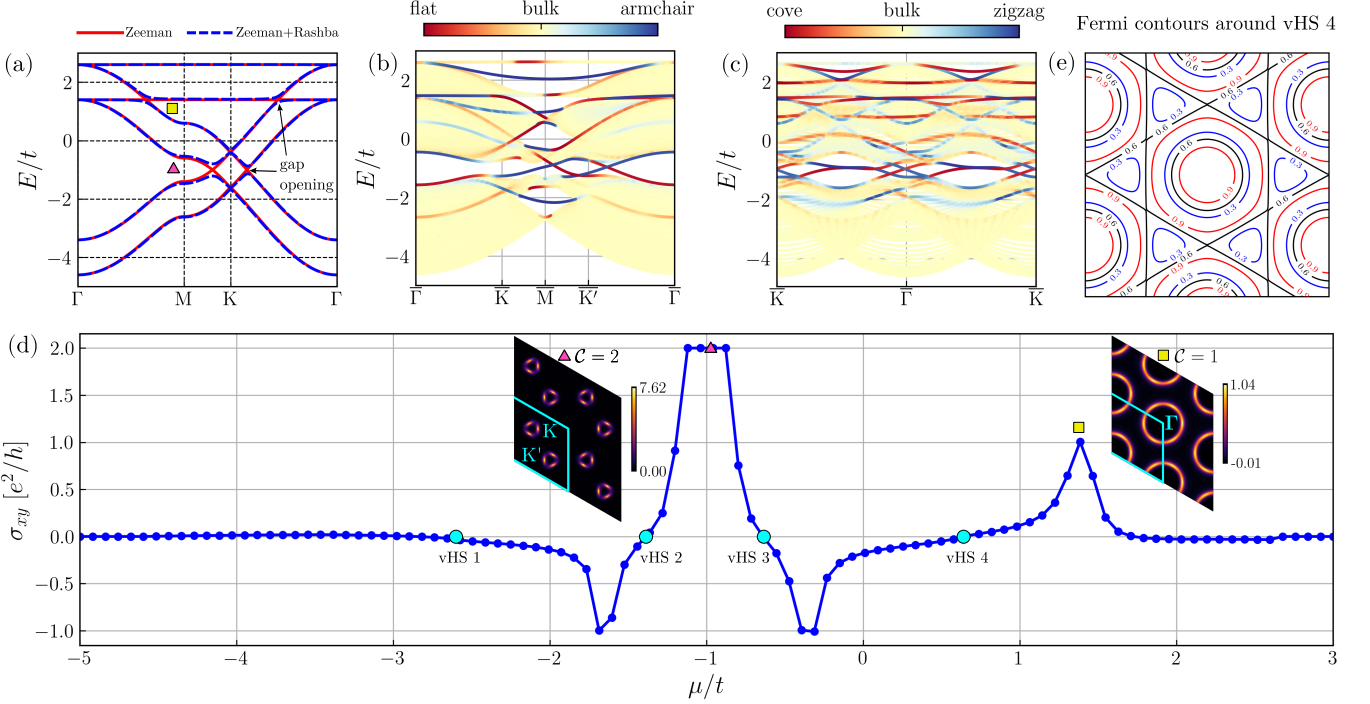


FIG. 4. (a) Bulk kagome bands for the QAH phase without (red) and with RSOC ($\lambda_R/t = 0.2$) (blue dashed) under constant Zeeman field ($h_z/t = 0.6$). Slab band structures with Zeeman and RSOC for (b) armchair-flat and (c) zigzag-cove terminations, with colors showing the expectation value of the position operator. (d) Anomalous Hall conductivity (in units of e^2/h) as a function of chemical potential. Circular cyan icons highlight the location of the VHS points. Insets show the Berry curvature maps in the two topological gaps, with icons also indicated in (a). Enclosed cyan line denote the BZ. (e) Fermi contours plotted at ($\mu/t = 0.6$) and around ($\mu/t = (0.3, 0.9)$) the VHS 4 in (d).

create a pair of DP and FB, as well as four VHS points. Applying RSOC mixes the spin channels and opens up a gap at the DP and FB. These bulk gaps host gapless edge states, which can be seen in the slab band structure in Fig. 4(b,c). Specifically, two pairs of edge states exist in the global gap around DP, whereas the pair of edge states near FB are less visible due to the small band gap.

The opening of a bulk gap and existence of edge states cannot verify non-trivial topology alone. We therefore also compute the intrinsic anomalous Hall conductance [73, 74]

$$\sigma_{xy}(E) = \frac{e^2}{h} \int_{BZ} \frac{d^2k}{A_{BZ}} \sum_n \Omega_{n,\mathbf{k}} \Theta(E_{n,\mathbf{k}} - E), \quad (15)$$

where Θ denotes the unit step function, E_n is the energy of the n -th band, A_{BZ} stands for the area of the BZ, and the Berry curvature is given by the formula

$$\Omega_{n,\mathbf{k}} = -\text{Im} \sum_{m \neq n} \frac{F_{mn,\mathbf{k}}^{xy} - F_{mn,\mathbf{k}}^{yx}}{(E_n - E_m)^2}, \quad (16)$$

$$F_{mn,\mathbf{k}}^{xy} = \langle u_n | \partial_{k_x} H_{\text{QAH}} | u_m \rangle \langle u_m | \partial_{k_y} H_{\text{QAH}} | u_n \rangle.$$

Breaking of TRS implies $\Omega_{n,\mathbf{k}} \neq \Omega_{n,-\mathbf{k}}$, which renders the anomalous conductance nonzero in Eq. (15) – a hallmark of QAH, where the Hall response is generated without the magnetic field. We plot σ_{xy} as a function of μ/t in

Fig. 4(d). The conductance becomes finite as more bands are filled, and exhibits a perfect quantized plateau around $\mu/t = -1$. This corresponds to the bulk gap around the DP [see pink triangle in Fig. 4(a,d)]. Inside a global topological QAH gap, the anomalous conductance is a constant given by $\sigma_{xy} = \mathcal{C}e^2/h$, where \mathcal{C} is the Chern number of the topological gap. Here we find $\mathcal{C} = 2$ for the gap around DP. Due to the bulk-boundary correspondence, this implies two protected edge states per edge, which can be seen in Fig. 4(b,c). Similarly, the narrow gap near the flat band [see yellow square in Fig. 4(a,d)] is topological with $\mathcal{C} = 1$, although the edge states are poorly resolved due to the small gap. Note that for the zigzag-cove termination, the BZ has a period given by $\bar{\Gamma}$ and \bar{K} , such that Fig. 4(c) displays the chiral modes twice. Also note that according to Fig. 2, the armchair-flat terminations are the top-bottom edges, while the cove-zigzag terminations are the left-right edges, respectively, which set how the Chern number sign determines the edge state dispersion.

The insets of Fig. 4(d) show the occupied Berry curvature at the two topological gaps. The map for $\mathcal{C} = 2$ contains satellite-like Berry curvature, with peaks concentrated near K and K' . Here, the lack of TRS ensures the satellite peaks are asymmetric between valleys. A less common pattern occurs for $\mathcal{C} = -1$, where the Berry

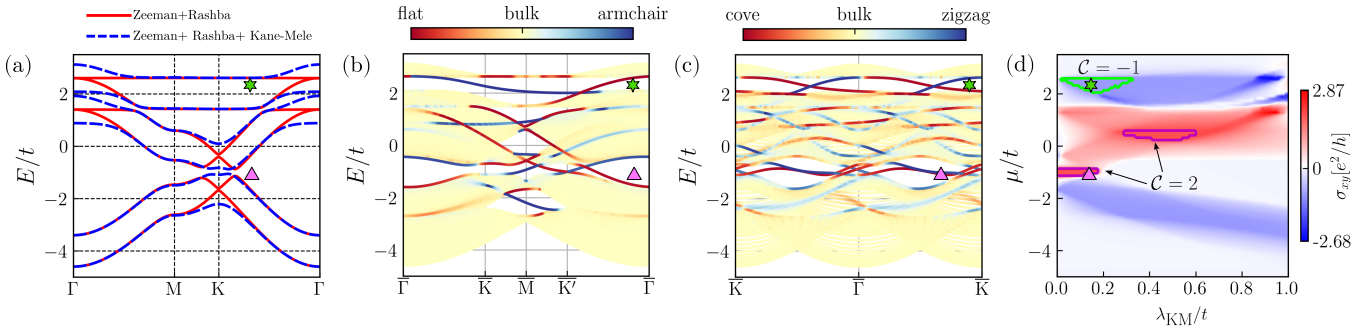


FIG. 5. (a) Bulk kagome bands for the QAH phase without (red) and with KMSOC ($\lambda_{\text{KM}}/t = 0.15$) (blue dashed) under constant Rashba SOC ($\lambda_R/t = 0.2$) and Zeeman field ($h_z/t = 0.6$). Slab band structures with Zeeman, RSOC, and KMSOC for (b) armchair-flat and (c) zigzag-cove terminations, with colors showing the expectation of the position operator. (d) Phase diagram capturing the evolution of the anomalous Hall conductivity σ_{xy} (in terms of e^2/h) as a function of chemical potential μ and Kane–Mele coupling λ_{KM} . Enclosed regions indicate quantized QAH phases with finite Chern number \mathcal{C} . In all plots, triangle and star icons refer to different topological gaps with $\mathcal{C} = 2$ and $\mathcal{C} = -1$, respectively.

curvature peaks form a ring around Γ . Other than these two global gaps, σ_{xy} sometimes shows a nearly quantized behavior. This is, however, not related to a finite Chern number since the system is here metallic, which makes the Chern number ill-defined.

Finally, we dedicate a few words on the relation between the change of sign in σ_{xy} and the Fermi surface (FS) topology. In Fig. 4(d), σ_{xy} changes sign at four points (cyan circles), which correspond to the VHS saddle points of the band structure. At these VHS, the FS abruptly changes its topology without necessarily breaking any symmetry. This is known as a Lifshitz transition [75, 76]. To illustrate this effect, we show the FS contour around VHS 4 in Fig. 4(e). The FS at the VHS reflects the lattice symmetry, forming hexagonal contours of maximal length that produce a diverging DOS. Below this filling ($\mu/t = 0.3$), we find a circular FSs around Γ and K/K' . One of these pockets disappear as the Fermi level is instead tuned above the VHS ($\mu/t = 0.9$). As a result, σ_{xy} can undergo a sign change at the VHS. Although we show the FS around VHS 4 here, the effect is similar at other VHS points.

B. Impact of Kane–Mele SOC

So far, we discussed how the RSOC opens topological Chern gaps in the spectrum. Here, we investigate how the Kane–Mele term modifies this topological landscape. If we focus on the bulk bands, we find in Fig. 5(a) that a finite KMSOC ($\lambda_{\text{KM}}/t = 0.15$) lifts point degeneracies at high symmetry points. The resulting gaps are different from those observed in the absence of KMSOC in Fig. 4(a). For example, a more clear gap opens up between the FB at Γ [see green star], while the gap at K also changes [see magnetia triangle]. These gaps are topological in nature. In fact, the Chern number for the first (triangle) gap is $\mathcal{C} = 2$, while for the latter (star)

is $\mathcal{C} = -1$. This is in agreement with the slab band structure in Fig. 5(b,c), where each gap hosts either one or two edge states per edge channel, consistent with the Chern number, with the Chern number sign determining the edge state dispersion.

Finally, we show the phase diagram in Fig. 5(d), by plotting the Hall conductance as a function of filling and Kane–Mele SOC strength. We identify quantization by the condition: $|\sigma_{xy} - \text{round}(\sigma_{xy})| < \epsilon$, where $\epsilon = 10^{-8}$ is a small number. The quantized regions of the phase diagram are marked with closed contours. For smaller KMSOC, both gaps near DP and FB remain topological with quantized anomalous conductance. As λ_{KM}/t is increased, the gaps around these energies become trivial, while instead a new quantized region appears close to $\mu/t = 0$.

VI. NON-COPLANAR MAGNETISM

Finally, we turn to the case where the QAH is driven by magnetic order other than FM. Due to the frustrated geometry of the kagome lattice, several exotic magnetic orderings are possible. The simplest scenario occurs when spins on three sublattices make 120° angle with respect to each other, forming a magnetic structure known as the $\mathbf{q} = 0$ order [41–44]. This is one of the allowed ground states of the antiferromagnetic Heisenberg model [41–43], where the magnetic unit cell coincides with the lattice unit cell. Although this magnetic order is coplanar, in real materials, Dzyaloshinskii–Moriya interaction [46, 77] can lead to out-of-plane spin canting. In fact, kagome minerals [78, 79] and thin films [80] are known to exhibit similar canting. Out-of-plane canting of spins forms a non-coplanar (NCL) magnetic order, which has direct consequences for the QAH phase. Particularly, scalar spin chirality [81], $\chi_{ijk} = \mathbf{S}_i \cdot (\mathbf{S}_j \times \mathbf{S}_k)$ ($i, j, k \in \text{NN sites}$), a quantity closely related to TRS breaking [82], becomes

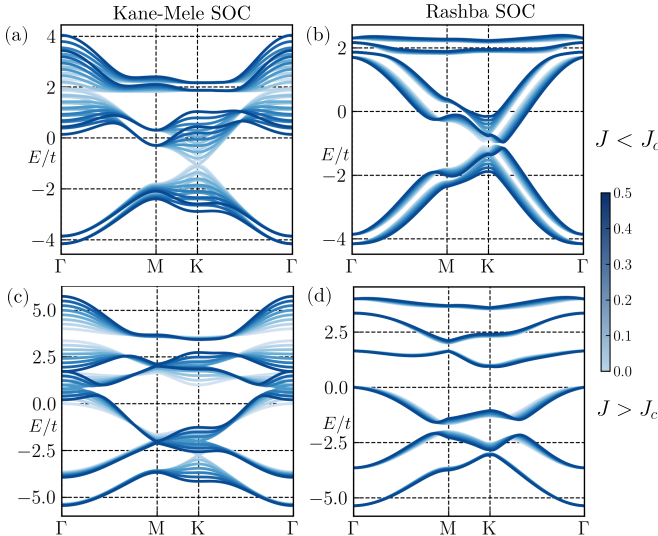


FIG. 6. Effect of (a,c) Kane–Mele and (b,d) Rashba SOC going from 0 to 0.5 (blue color) on the kagome bulk bands with non-coplanar $\mathbf{q} = 0$ magnetic order. Here, we consider two types of moments: $J = 0.3t < J_c$ (top panel) and $J = 2t > J_c$ (bottom panel). Parameters are $\mu/t = 0$, $\theta = \pi/3$, and $J_c/t \approx 1.51$.

finite for NCL ordering. In contrast, a coplanar configuration obtains $\chi_{ijk} = 0$. This makes the NCL magnetic order useful for realizing a QAH phase. In fact, previous works have predicted a QAH effect for NCL order within a Kondo-lattice model, where conduction electrons are coupled to localized spins via local exchange. The weak- [81] and strong-coupling [83] regimes can be solved analytically, but the intermediate regime [45] requires numerical solution. Despite these efforts, edge dispersion and SOC effects have been mostly neglected, which we address in this section.

To study the effects of a NCL magnetic structure, we consider the minimal local exchange Hamiltonian

$$H_{\text{NCL}} = -J_0 \sum_{i\sigma\sigma'} c_{i\sigma}^\dagger (\boldsymbol{\sigma}_{\sigma\sigma'} \cdot \mathbf{S}_i) c_{i\sigma'}, \quad (17)$$

where magnetic moments are defined in spherical coordinates as

$$\mathbf{S}_i = S (\sin \theta \cos \phi_i, \sin \theta \sin \phi_i, \cos \theta). \quad (18)$$

Here, $\phi_A = 0$, $\phi_B = 2\pi/3$, $\phi_C = -2\pi/3$ and θ denotes the polar angle. Furthermore, we define $J = J_0 S$ as the strength of the local exchange field. The bulk bands remain mostly gapless for small values of J/t ; however, larger values typically lift pointlike degeneracies and open gaps. Such gaps are topological in nature, which means the system can be turned into a Chern insulator with Fermi level tuning. Additionally, the Chern number of bands has been found to change when J crosses a critical value J_c , given by [45]

$$J_c(\theta)/t = \pm \frac{2}{\sqrt{1 + 3 \cos^2 \theta}}. \quad (19)$$

For our purposes, we choose the canting angle $\eta = \pi/6$, as observed in some kagome minerals [84], which sets $\theta = \pi/2 - \eta = \pi/3$. Thus, the limit $\theta = \pi/2$ (or $\eta = 0$) corresponds to the uncanted, coplanar structure. Plugging $\theta = \pi/3$ into Eq. (19) yields a critical value $J_c(\theta)/t \approx 1.51$ and we expect two sets of Chern phases in the subcritical ($J < J_c$) and supercritical ($J > J_c$) regimes.

The topological landscape is well understood without SOC, however, little is known when SOC is included. This motivates us to investigate SOC effects. To this end, we present the evolution of the bulk band structure with KMSOC and RSOC under a constant exchange field in Fig. 6. We consider two regimes of J : one below J_c ($J/t = 0.5$) and another above J_c ($J/t = 2$). Small J/t is in Fe-based [85] kagome materials with Hund's exchange $J_H/t \approx 0.25–0.37$, whereas kagome heavy-fermion [86] systems with larger moments and f electrons near Fermi level, are expected to show larger J/t . We find that tuning KMSOC in the presence of local moment significantly modifies the bands, which close/open gaps at different fillings. This behavior is present across all scales of J/t . In contrast, RSOC does not tune the bands nearly as much, and the energy gaps remain intact. This rules out any substantial role of RSOC in topological transitions, and we thus only focus on KMSOC.

In the subcritical regime, the KMSOC opens multiple global gaps [see Fig. 7(a)]. These gaps are then spin-split due to the exchange field. Similar to before, topological bulk gaps guarantee edge states for every termination [see shown in Fig. 7(b,c)]. Due to the size of the bulk gap, the edge states are more prominent near the DP, while the edge modes at higher energy, near the FB, hybridize with the bulk. To probe the non-triviality of the gaps, we plot the anomalous Hall conductivity as a function of filling and KMSOC in Fig. 7(d). We find two Chern insulating regions with $\mathcal{C} = -2$ (magenta triangle) and $\mathcal{C} = -1$ (green star), enclosed by magenta and green contours, respectively. Interestingly, the $\mathcal{C} = -2$ phase can occur without KMSOC, but a finite KMSOC is required for the $\mathcal{C} = -1$ phase that sits at higher energies. Increasing λ_{KM}/t transforms the chiral modes into helical-like modes, resulting in a vanishing Chern number (see Fig. SF2 in the SM [59]). An important difference between the Zeeman field and non-coplanar order is that the resulting Chern insulating phase at $1/3$ filling differs in sign, albeit with same magnitude. Note that we probe the phase diagram only up to $\lambda_{\text{KM}}/t = 0.3$ as no quantization is seen at higher values. This is commensurate with the scale of J/t .

For supercritical exchange fields, bands are mostly decoupled due to large splitting. Particularly, combination of exchange field and KMSOC leads to multiple global bulk gaps [see Fig. 7(e)]. The largest gap centered around zero energy is topologically trivial, whereas the remaining gaps are topological and are indicated by icons. Specifically, yellow square and green star symbols denote Chern phases with $\mathcal{C} = 1$ and $\mathcal{C} = -1$, respec-

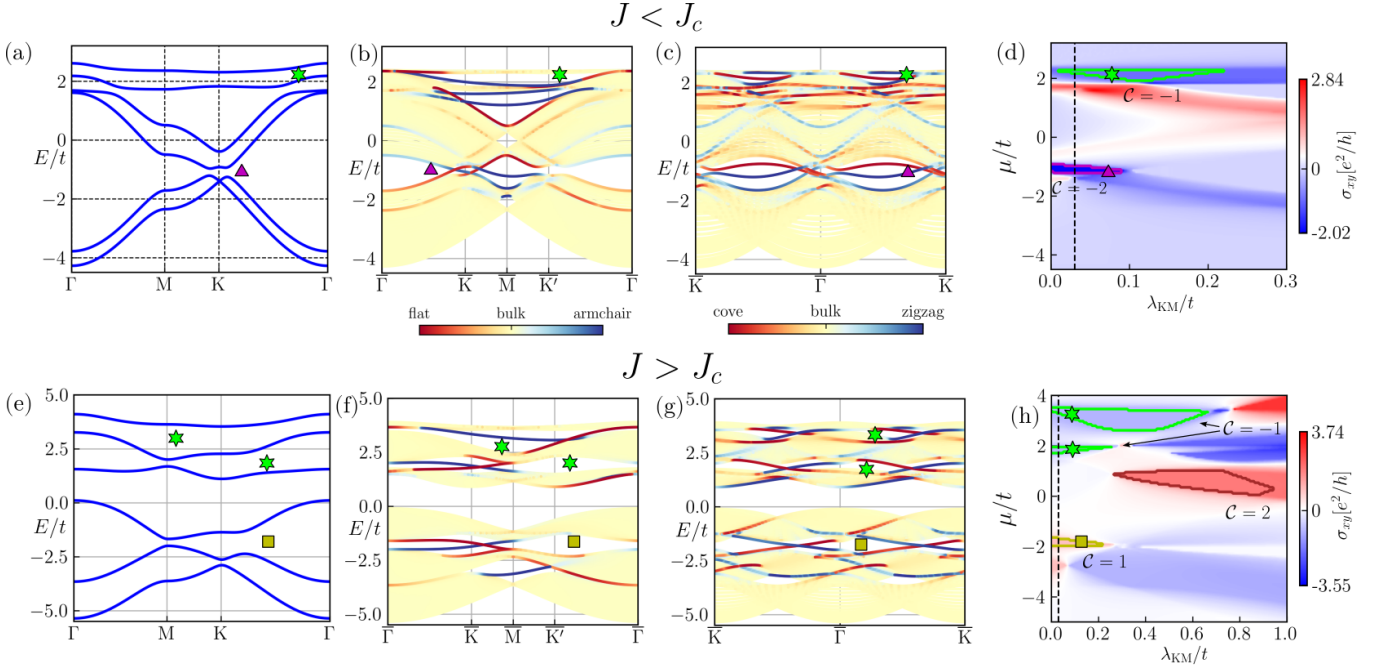


FIG. 7. Kagome bulk (a,e) and slab (b,c,f,g) band structure along with topological phase diagram (d,h) for subcritical $J/t = 0.5$ (top) and supercritical $J/t = 2$ (bottom) exchange fields. Colors in the slab band structure shows the expectation value of the position operator. Phase diagram shows the anomalous Hall conductivity σ_{xy} (in units of e^2/h) as a function of chemical potential μ and Kane–Mele coupling λ_{KM} . Enclosed regions indicate quantized QAH phases with finite Chern number \mathcal{C} . In all plots triangle, star, and square icons refer to different topological gaps with $\mathcal{C} = -2$, $\mathcal{C} = -1$, and $\mathcal{C} = 1$, respectively. Horizontal dashed line marks $\lambda_{KM}/t = 0.03$ used in the band-structure plots. Parameters are $\mu/t = 0$, $\theta = \pi/3$, and $J_c(\theta)/t \approx 1.51$.

tively [see Fig. 7(h)]. Same is corroborated by the slab band structures: each topological gap hosts a single co-propagating chiral edge mode, with its slope determined by $\text{sgn}(\mathcal{C})$ [see Fig. 7(f,g)]. Finally, the full Chern phase diagram is shown in Fig. 7(h). Owing to the large scale of J/t , the diagram extends up to $\lambda_{KM}/t = 1$. Consistent with the band structures, the phase diagram exhibits three topological regions with $\mathcal{C} = \pm 1$ at small KMSOC. As λ_{KM}/t increases, two of these regions are suppressed, while a distinct topological phase $\mathcal{C} = 2$ emerges and co-exists with the topmost $\mathcal{C} = -1$ phase. This behavior contrasts sharply with the subcritical regime, where increasing KMSOC completely eliminates all Chern phases.

VII. DISCUSSION AND CONCLUSION

In this work, we investigate edge states of the kagome lattice. Using a tight-binding framework, we carry out a systematic study of how factors like lattice termination, Kane–Mele and Rashba SOC, Zeeman field, and non-coplanar magnetic order affect the appearance and localization of edge modes. In the pristine limit, we find that the existence of edge states is highly sensitive to termination details: although most terminations guarantee physical edge modes, flat termination results in a complete absence of localized edge modes. Based on termina-

nation, there can also be valley mixing, leading to Dirac point-like dispersion at Γ .

Introducing Kane–Mele SOC significantly modifies the band structure by opening bulk gaps at the K and Γ points. When the Fermi level lies within these gaps, the system enters a quantum spin Hall insulating phase. This leads to a time-reversal-protected bulk topology, which guarantees spin-polarized, counter-propagating helical edge states in the slab spectrum, irrespective of termination. Unlike pristine edge states, helical modes are immune to backscattering due to time-reversal symmetry. The \mathbb{Z}_2 index quantifies the bulk topology, as confirmed through the odd winding of Wilson-loop eigenvalue phases across half of the Brillouin zone. We also note that termination-dependent trivial edge states may exist in the spectrum, which are not captured by the \mathbb{Z}_2 index.

In contrast, we find that the combination of a Zeeman field, mimicking a ferromagnetic configuration, with Rashba SOC drives the system into a quantum anomalous Hall phase under proper Fermi level tuning. This leads to two Chern insulating phases, $\mathcal{C} = 2$ and $\mathcal{C} = 1$. The bulk Chern number results in an equal number of co-propagating chiral edge states at the boundary. The bulk gap associated with the $\mathcal{C} = 1$ phase is relatively narrow, which limits the resolvability of the edge states. Small amounts of Kane–Mele SOC significantly widen this gap,

and flip $\mathcal{C} = 1$ to $\mathcal{C} = -1$, reversing the direction of chiral states. Further tuning of Kane–Mele coupling destroys the $\mathcal{C} = -1$ phase, while $\mathcal{C} = 2$ phase moves to a different filling.

In addition to a Zeeman field, a non-coplanar magnetic texture also leads to Chern phases since it yields a nonzero scalar spin chirality. Here, the canting angle of magnetic moments defines a critical exchange field at which the band Chern number changes and with that the edge state spectrum, creating two distinct exchange-field regimes. Regardless of this scale, Kane–Mele SOC modifies the bulk bands more strongly in the presence of a magnetic texture than Rashba SOC. At subcritical exchange fields, small Kane–Mele SOC yields two phases with $\mathcal{C} = -2$ and $\mathcal{C} = -1$. Although $\mathcal{C} = -2$ phase can be obtained with a magnetic texture alone, the $\mathcal{C} = -1$ phase requires Kane–Mele SOC. This landscape changes at supercritical fields, where three topological gaps open up with $\mathcal{C} = \pm 1$ for small amounts of Kane–Mele SOC. As SOC is increased, the Chern phases around $\mu/t = \pm 2$ disappear, and a new phase $\mathcal{C} = 2$ appears in the vicinity of $\mu/t = 0$. This is unlike the subcritical regime, where increasing SOC completely kills the Chern insulating phase.

In summary, we establish kagome lattice as a versatile platform for engineering tunable edge states. We identify four distinct lattice terminations, which can host up to five edge states. The edge state spectra depend strongly on the termination, possibly explaining distinct edge and surface features observed for different cleaves or terraces [29, 30]. Certain terminations suppress edge modes or induce valley mixing, with implications for surface and interface engineering. The pristine system hosts trivial edge states embedded in a gapless bulk spectrum, which can be gapped by SOC. In particular, Kane–Mele SOC generates a pair of helical edge modes for in-gap fillings, independent of termination. Such heli-

cal modes are expected in nonmagnetic kagome metals such as CsV_3Sb_5 [19, 87] and KV_3Sb_5 [20]. When time-reversal symmetry is broken, either by ferromagnetism or non-coplanar magnetic order, bulk Chern gaps emerge with gapless chiral edge modes. Ferromagnetism requires Rashba SOC to open topological gaps, a combination naturally realized in magnetic kagome materials such as $\text{Co}_3\text{Sn}_2\text{S}_2$ [88], TbMn_6Sn_6 [89], and FeGe [30]. By contrast, non-coplanar magnetic order, as in Mn_3Sn [90, 91], MnBi_2Te_4 [92], and CoM_3S_6 ($\text{M} = \text{Nb}, \text{Ta}$) [93], generates distinct Chern phases depending on the exchange field. In both scenarios, Kane–Mele SOC provides an additional control knob, enabling tuning or destruction of Chern phases. Our results are directly relevant for surface engineering, tailored edge transport, or device-oriented topological functionality in kagome-based materials.

ACKNOWLEDGMENTS

S.S. acknowledges the financial support provided by the Polish National Agency for Academic Exchange NAWA under the Programme STER-Internationalisation of doctoral schools, Project no BPI/STE/2023/1/00027/U/00001. S.S. is also grateful for the hospitality and support provided by the Department of Physics and Astronomy at Uppsala University during the early stages of this work. S.S. and A.P. further acknowledge support from the National Science Centre (NCN, Poland) under Project No. 2021/43/B/ST3/02166. A.B.S. acknowledges financial support from the Swedish Research Council (Vetenskapsrådet) Grant No. 2022-03963. We gratefully acknowledge Polish high-performance computing infrastructure PLGrid (HPC Center: ACK Cyfronet AGH) for providing computer facilities and support within computational grant no. PLG/2024/017875.

[1] Y. Hatsugai, Chern number and edge states in the integer quantum Hall effect, *Phys. Rev. Lett.* **71**, 3697 (1993).

[2] K. Matan, D. Grohol, D. G. Nocera, T. Yildirim, A. B. Harris, S. H. Lee, S. E. Nagler, and Y. S. Lee, Spin waves in the frustrated kagomé lattice antiferromagnet $\text{KFe}_3(\text{OH})_6(\text{SO}_4)_2$, *Phys. Rev. Lett.* **96**, 247201 (2006).

[3] R. Moessner and S. L. Sondhi, Ising models of quantum frustration, *Phys. Rev. B* **63**, 224401 (2001).

[4] M. Hermele, M. P. A. Fisher, and L. Balents, Pyrochlore photons: The $U(1)$ spin liquid in a $S = \frac{1}{2}$ three-dimensional frustrated magnet, *Phys. Rev. B* **69**, 064404 (2004).

[5] L. Balents, M. P. A. Fisher, and S. M. Girvin, Fractionalization in an easy-axis kagome antiferromagnet, *Phys. Rev. B* **65**, 224412 (2002).

[6] T.-H. Han, J. S. Helton, S. Chu, D. G. Nocera, J. A. Rodriguez-Rivera, C. Broholm, and Y. S. Lee, Fractionalized excitations in the spin-liquid state of a kagome-lattice antiferromagnet, *Nature* **492**, 406 (2012).

[7] X. Teng, L. Chen, F. Ye, E. Rosenberg, Z. Liu, J.-X. Yin, Y.-X. Jiang, J. S. Oh, M. Z. Hasan, K. J. Neubauer, B. Gao, Y. Xie, M. Hashimoto, D. Lu, C. Jozwiak, A. Bostwick, E. Rotenberg, R. J. Birgeneau, J.-H. Chu, M. Yi, and P. Dai, Discovery of charge density wave in a kagome lattice antiferromagnet, *Nature* **609**, 490 (2022).

[8] H. Tan, Y. Liu, Z. Wang, and B. Yan, Charge density waves and electronic properties of superconducting kagome metals, *Phys. Rev. Lett.* **127**, 046401 (2021).

[9] A. Ptak, A. Kobiałka, M. Sternik, J. Łazewski, P. T. Jochym, A. M. Oleś, and P. Piekarz, Dynamical study of the origin of the charge density wave in $AV_3\text{Sb}_5$ ($A = \text{K}, \text{Rb}, \text{Cs}$) compounds, *Phys. Rev. B* **105**, 235134 (2022).

[10] P. Park, B. R. Ortiz, M. Sprague, A. P. Sakhya, S. A. Chen, M. D. Frontzek, W. Tian, R. Sibille, D. G. Mazzone, C. Tabata, K. Kaneko, L. M. DeBeer-Schmitt, M. B. Stone, D. S. Parker, G. D. Samolyuk, H. Miao, M. Neupane, and A. D. Christianson, Spin density wave and van Hove singularity in the kagome metal CeTi_3Bi_4 ,

Nat. Commun. **16**, 4384 (2025).

[11] H. Chen, H. Yang, B. Hu, Z. Zhao, J. Yuan, Y. Xing, G. Qian, Z. Huang, G. Li, Y. Ye, S. Ma, S. Ni, H. Zhang, Q. Yin, C. Gong, Z. Tu, H. Lei, H. Tan, S. Zhou, C. Shen, X. Dong, B. Yan, Z. Wang, and H.-J. Gao, Roton pair density wave in a strong-coupling kagome superconductor, *Nature* **599**, 222 (2021).

[12] H. Yang, Y. Ye, Z. Zhao, J. Liu, X.-W. Yi, Y. Zhang, H. Xiao, J. Shi, J.-Y. You, Z. Huang, B. Wang, J. Wang, H. Guo, X. Lin, C. Shen, W. Zhou, H. Chen, X. Dong, G. Su, Z. Wang, and H.-J. Gao, Superconductivity and nematic order in a new titanium-based kagome metal CsTi_3Bi_5 without charge density wave order, *Nat. Commun.* **15**, 9626 (2024).

[13] T. Asaba, A. Onishi, Y. Kageyama, T. Kiyosue, K. Ohtsuka, S. Suetsugu, Y. Kohsaka, T. Gaggl, Y. Kasahara, H. Murayama, K. Hashimoto, R. Tazai, H. Kontani, B. R. Ortiz, S. D. Wilson, Q. Li, H. H. Wen, T. Shibauchi, and Y. Matsuda, Evidence for an odd-parity nematic phase above the charge-density-wave transition in a kagome metal, *Nat. Phys.* **20**, 40 (2024).

[14] L. Nie, K. Sun, W. Ma, D. Song, L. Zheng, Z. Liang, P. Wu, F. Yu, J. Li, M. Shan, D. Zhao, S. Li, B. Kang, Z. Wu, Y. Zhou, K. Liu, Z. Xiang, J. Ying, Z. Wang, T. Wu, and X. Chen, Charge-density-wave-driven electronic nematicity in a kagome superconductor, *Nature* **604**, 59 (2022).

[15] Y. Xu, Z. Ni, Y. Liu, B. R. Ortiz, Q. Deng, S. D. Wilson, B. Yan, L. Balents, and L. Wu, Three-state nematicity and magneto-optical kerr effect in the charge density waves in kagome superconductors, *Nat. Phys.* **18**, 1470 (2022).

[16] M. Hirschberger, T. Nakajima, S. Gao, L. Peng, A. Kikkawa, T. Kurumaji, M. Kriener, Y. Yamasaki, H. Sagayama, H. Nakao, K. Ohishi, K. Kakurai, Y. Taguchi, X. Yu, T.-h. Arima, and Y. Tokura, Skyrmion phase and competing magnetic orders on a breathing kagomé lattice, *Nat. Commun.* **10**, 5831 (2019).

[17] M. Hirschberger, B. G. Szigeti, M. Hemmida, M. M. Hirschmann, S. Esser, H. Ohsumi, Y. Tanaka, L. Spitz, S. Gao, K. K. Kolincio, H. Sagayama, H. Nakao, Y. Yamasaki, L. Forró, H.-A. Krug von Nidda, I. Kezsmarki, T.-h. Arima, and Y. Tokura, Lattice-commensurate skyrmion texture in a centrosymmetric breathing kagome magnet, *npj Quantum Mater.* **9**, 45 (2024).

[18] C. Mielke, D. Das, J.-X. Yin, H. Liu, R. Gupta, Y.-X. Jiang, M. Medarde, X. Wu, H. C. Lei, J. Chang, P. Dai, Q. Si, H. Miao, R. Thomale, T. Neupert, Y. Shi, R. Khasanov, M. Z. Hasan, H. Luetkens, and Z. Guguchia, Time-reversal symmetry-breaking charge order in a kagome superconductor, *Nature* **602**, 245 (2022).

[19] B. R. Ortiz, S. M. L. Teicher, Y. Hu, J. L. Zuo, P. M. Sarte, E. C. Schueller, A. M. M. Abeykoon, M. J. Krogstad, S. Rosenkranz, R. Osborn, R. Seshadri, L. Balents, J. He, and S. D. Wilson, CsV_3Sb_5 : A Z_2 topological kagome metal with a superconducting ground state, *Phys. Rev. Lett.* **125**, 247002 (2020).

[20] B. R. Ortiz, P. M. Sarte, E. M. Kenney, M. J. Graf, S. M. L. Teicher, R. Seshadri, and S. D. Wilson, Superconductivity in the \mathbb{Z}_2 kagome metal KV_3Sb_5 , *Phys. Rev. Mater.* **5**, 034801 (2021).

[21] Z. Guguchia, C. Mielke, D. Das, R. Gupta, J.-X. Yin, H. Liu, Q. Yin, M. H. Christensen, Z. Tu, C. Gong, N. Shumiya, M. S. Hossain, T. Gamsakhurdashvili, M. Elender, P. Dai, A. Amato, Y. Shi, H. C. Lei, R. M. Fernandes, M. Z. Hasan, H. Luetkens, and R. Khasanov, Tunable unconventional kagome superconductivity in charge ordered RbV_3Sb_5 and KV_3Sb_5 , *Nat. Commun.* **14**, 153 (2023).

[22] K. Nakada, M. Fujita, G. Dresselhaus, and M. S. Dresselhaus, Edge state in graphene ribbons: Nanometer size effect and edge shape dependence, *Phys. Rev. B* **54**, 17954 (1996).

[23] M. Fujita, K. Wakabayashi, K. Nakada, and K. Kusakabe, Peculiar localized state at zigzag graphite edge, *J. Phys. Soc. Jpn.* **65**, 1920 (1996).

[24] Y.-W. Son, M. L. Cohen, and S. G. Louie, Half-metallic graphene nanoribbons, *Nature* **444**, 347 (2006).

[25] A. García-Fuente, D. Carrascal, G. Ross, and J. Ferrer, Full analytical solution of finite-length armchair/zigzag nanoribbons, *Phys. Rev. B* **107**, 115403 (2023).

[26] G.-P. Guo, Z.-R. Lin, T. Tu, G. Cao, X.-P. Li, and G.-C. Guo, Quantum computation with graphene nanoribbon, *New J. Phys.* **11**, 123005 (2009).

[27] Y. Li, Z. Zhou, C. R. Cabrera, and Z. Chen, Preserving the edge magnetism of zigzag graphene nanoribbons by ethylene termination: Insight by Clar's rule, *Sci. Rep.* **3**, 2030 (2013).

[28] O. V. Zakhарова, E. E. Mastalygina, K. S. Golokhvast, and A. A. Gusev, Graphene Nanoribbons: Prospects of Application in Biomedicine and Toxicity, *Nanomaterials* **11**, 2425 (2021).

[29] F. Mazzola, S. Enzner, P. Eck, C. Bigi, M. Jugovac, I. Cojocariu, V. Feyer, Z. Shu, G. M. Pierantozzi, A. De Vita, P. Carrara, J. Fujii, P. D. C. King, G. Vinai, P. Orgiani, C. Cacho, M. D. Watson, G. Rossi, I. Vobornik, T. Kong, D. Di Sante, G. Sangiovanni, and G. Panaccione, Observation of termination-dependent topological connectivity in a magnetic Weyl kagome lattice, *Nano Lett.* **23**, 8035 (2023).

[30] J.-X. Yin, Y.-X. Jiang, X. Teng, M. S. Hossain, S. Mardanya, T.-R. Chang, Z. Ye, G. Xu, M. M. Denner, T. Neupert, B. Lienhard, H.-B. Deng, C. Setty, Q. Si, G. Chang, Z. Guguchia, B. Gao, N. Shumiya, Q. Zhang, T. A. Cochran, D. Multer, M. Yi, P. Dai, and M. Z. Hasan, Discovery of charge order and corresponding edge state in kagome magnet FeGe , *Phys. Rev. Lett.* **129**, 166401 (2022).

[31] G. Liu, T. Yang, Y.-X. Jiang, S. Hossain, H. Deng, M. Z. Hasan, and J.-X. Yin, Perspective: imaging atomic step geometry to determine surface terminations of kagome materials and beyond, *Quantum Front.* **3**, 19 (2024).

[32] Y.-L. Sun, G.-H. Chen, S.-C. Du, Z.-B. Chen, Y.-W. Zhou, and E.-J. Ye, Spin-valley polarized edge states in quasi-one-dimensional asymmetric kagome lattice, *Front. Phys.* **10**, 1033836 (2022).

[33] C. L. Kane and E. J. Mele, Quantum spin Hall effect in graphene, *Phys. Rev. Lett.* **95**, 226801 (2005).

[34] E. Liu, Y. Sun, N. Kumar, L. Muechler, A. Sun, L. Jiao, S.-Y. Yang, D. Liu, A. Liang, Q. Xu, J. Kroder, V. Süß, H. Borrman, C. Shekhar, Z. Wang, C. Xi, W. Wang, W. Schnelle, S. Wirth, Y. Chen, S. T. B. Goennenwein, and C. Felser, Giant anomalous Hall effect in a ferromagnetic kagome-lattice semimetal, *Nat. Phys.* **14**, 1125 (2018).

[35] H. Tanaka, Y. Fujisawa, K. Kuroda, R. Noguchi,

S. Sakuragi, C. Bareille, B. Smith, C. Cacho, S. W. Jung, T. Muro, Y. Okada, and T. Kondo, Three-dimensional electronic structure in ferromagnetic Fe_3Sn_2 with breathing kagome bilayers, *Phys. Rev. B* **101**, 161114 (2020).

[36] L. Ye, M. Kang, J. Liu, F. von Cube, C. R. Wicker, T. Suzuki, C. Jozwiak, A. Bostwick, E. Rotenberg, D. C. Bell, L. Fu, R. Comin, and J. G. Checkelsky, Massive Dirac fermions in a ferromagnetic kagome metal, *Nature* **555**, 638 (2018).

[37] Y. Zhou, M.-K. Lee, S. Hammouda, S. Devi, S.-I. Yano, R. Sibile, O. Zaharko, W. Schmidt, K. Schmalzl, K. Beauvois, E. Ressouche, P.-C. Chang, C.-H. Huang, L.-J. Chang, T. Brückel, and Y. Su, Ground-state magnetic structures of topological kagome metals $RV_6\text{Sn}_6$ ($R = \text{Tb, Dy, Ho, Er}$), *Phys. Rev. Res.* **6**, 043291 (2024).

[38] R. M. Lutchyn, J. D. Sau, and S. Das Sarma, Majorana fermions and a topological phase transition in semiconductor-superconductor heterostructures, *Phys. Rev. Lett.* **105**, 077001 (2010).

[39] C. Nayak, S. H. Simon, A. Stern, M. Freedman, and S. Das Sarma, Non-Abelian anyons and topological quantum computation, *Rev. Mod. Phys.* **80**, 1083 (2008).

[40] P. W. Shor, Fault-tolerant quantum computation (1996), [arXiv:quant-ph/9605011](https://arxiv.org/abs/quant-ph/9605011).

[41] A. Chubukov, Order from disorder in a kagomé antiferromagnet, *Phys. Rev. Lett.* **69**, 832 (1992).

[42] A. B. Harris, C. Kallin, and A. J. Berlinsky, Possible Néel orderings of the kagomé antiferromagnet, *Phys. Rev. B* **45**, 2899 (1992).

[43] O. Götze, D. J. J. Farnell, R. F. Bishop, P. H. Y. Li, and J. Richter, Heisenberg antiferromagnet on the kagome lattice with arbitrary spin: A higher-order coupled cluster treatment, *Phys. Rev. B* **84**, 224428 (2011).

[44] J. Watanabe, Y. Araki, K. Kobayashi, A. Ozawa, and K. Nomura, Magnetic orderings from spin-orbit coupled electrons on kagome lattice, *J. Phys. Soc. Jpn.* **91**, 083702 (2022).

[45] M. Taillefumier, B. Canals, C. Lacroix, V. K. Dugaev, and P. Bruno, Anomalous Hall effect due to spin chirality in the kagomé lattice, *Phys. Rev. B* **74**, 085105 (2006).

[46] M. Elhajal, B. Canals, and C. Lacroix, Symmetry breaking due to Dzyaloshinsky-Moriya interactions in the kagomé lattice, *Phys. Rev. B* **66**, 014422 (2002).

[47] A. Bolens and N. Nagaosa, Topological states on the breathing kagome lattice, *Phys. Rev. B* **99**, 165141 (2019).

[48] S. Fang, L. Ye, M. P. Ghimire, M. Kang, J. Liu, M. Han, L. Fu, M. Richter, J. van den Brink, E. Kaxiras, R. Comin, and J. G. Checkelsky, Ferromagnetic helical nodal line and Kane-Mele spin-orbit coupling in kagome metal Fe_3Sn_2 , *Phys. Rev. B* **105**, 035107 (2022).

[49] I. Titvinidze, J. Legendre, K. Le Hur, and W. Hofstetter, Hubbard model on the kagome lattice with time-reversal invariant flux and spin-orbit coupling, *Phys. Rev. B* **105**, 235102 (2022).

[50] O. Busch, I. Mertig, and B. Göbel, Orbital Hall effect and orbital edge states caused by s electrons, *Phys. Rev. Res.* **5**, 043052 (2023).

[51] L. Ye, M. K. Chan, R. D. McDonald, D. Graf, M. Kang, J. Liu, T. Suzuki, R. Comin, L. Fu, and J. G. Checkelsky, de Haas-van Alphen effect of correlated Dirac states in kagome metal Fe_3Sn_2 , *Nat. Commun.* **10**, 4870 (2019).

[52] D. Di Sante, C. Bigi, P. Eck, S. Enzner, A. Consiglio, G. Pokharel, P. Carrara, P. Orgiani, V. Polewczuk, J. Fu-
jii, P. D. C. King, I. Vobornik, G. Rossi, I. Zeljkovic, S. D. Wilson, R. Thomale, G. Sangiovanni, G. Panaccione, and F. Mazzola, Flat band separation and robust spin Berry curvature in bilayer kagome metals, *Nat. Phys.* **19**, 1135 (2023).

[53] S. Sajid and A. Chakrabarti, Localization, transport, and edge states in a two-strand ladder network in an aperiodically staggered magnetic field, *Phys. Rev. B* **102**, 134401 (2020).

[54] C. L. Kane and E. J. Mele, Z_2 topological order and the quantum spin hall effect, *Phys. Rev. Lett.* **95**, 146802 (2005).

[55] R. Yu, X. L. Qi, A. Bernevig, Z. Fang, and X. Dai, Equivalent expression of \mathbb{Z}_2 topological invariant for band insulators using the non-Abelian Berry connection, *Phys. Rev. B* **84**, 075119 (2011).

[56] A. Alexandradinata, X. Dai, and B. A. Bernevig, Wilson-loop characterization of inversion-symmetric topological insulators, *Phys. Rev. B* **89**, 155114 (2014).

[57] A. A. Soluyanov and D. Vanderbilt, Wannier representation of \mathbb{Z}_2 topological insulators, *Phys. Rev. B* **83**, 035108 (2011).

[58] A. A. Soluyanov and D. Vanderbilt, Computing topological invariants without inversion symmetry, *Phys. Rev. B* **83**, 235401 (2011).

[59] See Supplemental Material at [URL will be inserted by publisher] for additional theoretical results.

[60] Y. Yang, Z. Xu, L. Sheng, B. Wang, D. Y. Xing, and D. N. Sheng, Time-reversal-symmetry-broken quantum spin Hall effect, *Phys. Rev. Lett.* **107**, 066602 (2011).

[61] C.-Z. Chang, J. Zhang, X. Feng, J. Shen, Z. Zhang, M. Guo, K. Li, Y. Ou, P. Wei, L.-L. Wang, Z.-Q. Ji, Y. Feng, S. Ji, X. Chen, J. Jia, X. Dai, Z. Fang, S.-C. Zhang, K. He, Y. Wang, L. Lu, X.-C. Ma, and Q.-K. Xue, Experimental observation of the quantum anomalous Hall effect in a magnetic topological insulator, *Science* **340**, 167 (2013).

[62] D. Chen, C. Le, C. Fu, H. Lin, W. Schnelle, Y. Sun, and C. Felser, Large anomalous Hall effect in the kagome ferromagnet LiMn_6Sn_6 , *Phys. Rev. B* **103**, 144410 (2021).

[63] A. Mielke, Ferromagnetism in single-band Hubbard models with a partially flat band, *Phys. Rev. Lett.* **82**, 4312 (1999).

[64] E. C. Stoner, Collective electron ferromagnetism, *Proc. R. Soc. Lond. A* **165**, 372 (1938).

[65] K. Kuroda, T. Tomita, M.-T. Suzuki, C. Bareille, A. A. Nugroho, P. Goswami, M. Ochi, M. Ikhlas, M. Nakayama, S. Akebi, R. Noguchi, R. Ishii, N. Inami, K. Ono, H. Kumigashira, A. Varykhalov, T. Muro, T. Koretsune, R. Arita, S. Shin, T. Kondo, and S. Nakatsuji, Evidence for magnetic Weyl fermions in a correlated metal, *Nature Mater.* **16**, 1090 (2017).

[66] D. F. Liu, E. K. Liu, Q. N. Xu, J. L. Shen, Y. W. Li, D. Pei, A. J. Liang, P. Dudin, T. K. Kim, C. Cacho, Y. F. Xu, Y. Sun, L. X. Yang, Z. K. Liu, C. Felser, S. S. P. Parkin, and Y. L. Chen, Direct observation of the spin-orbit coupling effect in magnetic Weyl semimetal $\text{Co}_3\text{Sn}_2\text{S}_2$, *npj Quantum Mater.* **7**, 11 (2022).

[67] S. Sekh and I. Mandal, Magnus Hall effect in three-dimensional topological semimetals, *Eur. Phys. J. Plus* **137**, 736 (2022).

[68] D. J. Thouless, M. Kohmoto, M. P. Nightingale, and M. den Nijs, Quantized Hall conductance in a two-dimensional periodic potential, *Phys. Rev. Lett.* **49**, 405

(1982).

[69] F. D. M. Haldane, Model for a quantum Hall effect without Landau levels: Condensed-matter realization of the “parity anomaly”, *Phys. Rev. Lett.* **61**, 2015 (1988).

[70] R. Yu, W. Zhang, H.-J. Zhang, S.-C. Zhang, X. Dai, and Z. Fang, Quantized anomalous Hall effect in magnetic topological insulators, *Science* **329**, 61 (2010).

[71] Z. Qiao, S. A. Yang, W. Feng, W.-K. Tse, J. Ding, Y. Yao, J. Wang, and Q. Niu, Quantum anomalous Hall effect in graphene from Rashba and exchange effects, *Phys. Rev. B* **82**, 161414 (2010).

[72] J. Ding, Z. Qiao, W. Feng, Y. Yao, and Q. Niu, Engineering quantum anomalous/valley Hall states in graphene via metal-atom adsorption: An ab-initio study, *Phys. Rev. B* **84**, 195444 (2011).

[73] T. Jungwirth, Q. Niu, and A. H. MacDonald, Anomalous Hall effect in ferromagnetic semiconductors, *Phys. Rev. Lett.* **88**, 207208 (2002).

[74] N. Nagaosa, J. Sinova, S. Onoda, A. H. MacDonald, and N. P. Ong, Anomalous Hall effect, *Rev. Mod. Phys.* **82**, 1539 (2010).

[75] I. M. Lifshitz, Anomalies of electron characteristics of a metal in the high pressure region, *Soviet Physics JETP* **11**, 1130 (1960).

[76] G. E. Volovik, Topological Lifshitz transitions, *Low Temp. Phys.* **43**, 47 (2017).

[77] B. Li, S. Sandhoefner, and A. A. Kovalev, Intrinsic spin Nernst effect of magnons in a noncollinear antiferromagnet, *Phys. Rev. Res.* **2**, 013079 (2020).

[78] T. Yildirim and A. B. Harris, Magnetic structure and spin waves in the kagomé jarosite compound $KFe_3(SO_4)_2(OH)_6$, *Phys. Rev. B* **73**, 214446 (2006).

[79] A. Verrier, F. Bert, J. M. Parent, M. El-Amine, J. C. Orain, D. Boldrin, A. S. Wills, P. Mendels, and J. A. Quilliam, Canted antiferromagnetic order in the kagomé material Sr-vesignieite, *Phys. Rev. B* **101**, 054425 (2020).

[80] K. Fujiwara, Y. Kato, T. Seki, K. Nomura, K. Takanashi, Y. Motome, and A. Tsukazaki, Tuning scalar spin chirality in ultrathin films of the kagomé-lattice ferromagnet Fe_3Sn , *Commun. Mater.* **2**, 113 (2021).

[81] G. Tatara and H. Kawamura, Chirality-driven anomalous Hall effect in weak coupling regime, *J. Phys. Soc. Jpn.* **71**, 2613 (2002).

[82] X. G. Wen, F. Wilczek, and A. Zee, Chiral spin states and superconductivity, *Phys. Rev. B* **39**, 11413 (1989).

[83] K. Ohgushi, S. Murakami, and N. Nagaosa, Spin anisotropy and quantum Hall effect in the kagomé lattice: Chiral spin state based on a ferromagnet, *Phys. Rev. B* **62**, R6065 (2000).

[84] P. Laurell and G. A. Fiete, Magnon thermal Hall effect in kagomé antiferromagnets with Dzyaloshinskii-Moriya interactions, *Phys. Rev. B* **98**, 094419 (2018).

[85] W. Zhang, T. C. Asmara, Y. Tseng, J. Li, Y. Xiong, Y. Wei, T. Yu, C. W. Galdino, Z. Zhang, K. Kummer, V. N. Strocov, Y. Soh, T. Schmitt, and G. Aeppli, Spin waves and orbital contribution to ferromagnetism in a topological metal, *Nat. Commun.* **15**, 8905 (2024).

[86] B. Song, Y. Xie, W.-J. Li, H. Liu, J. Chen, S. Tian, X. Zhang, Q. Wang, X. Li, H. Lei, Q. Zhang, J.-g. Guo, L. Zhao, S.-L. Yu, X. Zhou, X. Chen, and T. Ying, Realization of kagomé Kondo lattice, *Nat. Commun.* **16**, 5643 (2025).

[87] Y. Hu, S. M. Teicher, B. R. Ortiz, Y. Luo, S. Peng, L. Huai, J. Ma, N. C. Plumb, S. D. Wilson, J. He, and M. Shi, Topological surface states and flat bands in the kagomé superconductor CsV_3Sb_5 , *Sci. Bull.* **67**, 495 (2022).

[88] S. Howard, L. Jiao, Z. Wang, N. Morali, R. Batabyal, P. Kumar-Nag, N. Avraham, H. Beidenkopf, P. Vir, E. Liu, C. Shekhar, C. Felser, T. Hughes, and V. Madhavan, Evidence for one-dimensional chiral edge states in a magnetic Weyl semimetal $Co_3Sn_2S_2$, *Nat. Commun.* **12**, 4269 (2021).

[89] J.-X. Yin, W. Ma, T. A. Cochran, X. Xu, S. S. Zhang, H.-J. Tien, N. Shumiya, G. Cheng, K. Jiang, B. Lian, Z. Song, G. Chang, I. Belopolski, D. Multer, M. Litskevich, Z.-J. Cheng, X. P. Yang, B. Swidler, H. Zhou, H. Lin, T. Neupert, Z. Wang, N. Yao, T.-R. Chang, S. Jia, and M. Zahid Hasan, Quantum-limit Chern topological magnetism in $TbMn_6Sn_6$, *Nature* **583**, 533 (2020).

[90] X. Li, J. Koo, Z. Zhu, K. Behnia, and B. Yan, Field-linear anomalous Hall effect and Berry curvature induced by spin chirality in the kagomé antiferromagnet Mn_3Sn , *Nat. Commun.* **14**, 1642 (2023).

[91] A. Low, S. Ghosh, and S. Thirupathaiah, Topological Hall effect instigated in kagomé $Mn_{3-x}Sn$ due to Mn-deficit induced noncoplanar spin structure, *J. Phys.: Condens. Matter* **37**, 065701 (2024).

[92] H. Yang, J. Huang, S. Tian, K. Xia, Z. Wang, Y. Zhang, J. Ma, H. Guo, X. Zhang, J. Dai, Y. Luo, S. Wang, H. Lei, and Y. Li, Observation of topological Hall effect and Nernst effect in the canted antiferromagnetic phase of $MnBi_2Te_4$, *Chinese Phys. Lett.* **42**, 080706 (2025).

[93] H. Takagi, R. Takagi, S. Minami, T. Nomoto, K. Ohishi, M.-T. Suzuki, Y. Yanagi, M. Hirayama, N. D. Khanh, K. Karube, H. Saito, D. Hashizume, R. Kiyanagi, Y. Tokura, R. Arita, T. Nakajima, and S. Seki, Spontaneous topological Hall effect induced by non-coplanar antiferromagnetic order in intercalated van der Waals materials, *Nat. Phys.* **19**, 961 (2023).

Supplemental Material

Kagome edge states under lattice termination, spin–orbit coupling, and magnetic order

Sajid Sekh¹, Annica M. Black-Schaffer², and Andrzej Ptok¹

¹*Institute of Nuclear Physics, Polish Academy of Sciences, W. E. Radzikowskiego 152, PL-31342 Kraków, Poland*

²*Department of Physics and Astronomy, Uppsala University, Box 516, S-751 20 Uppsala, Sweden*

SM1. ADDITIONAL FIGURES

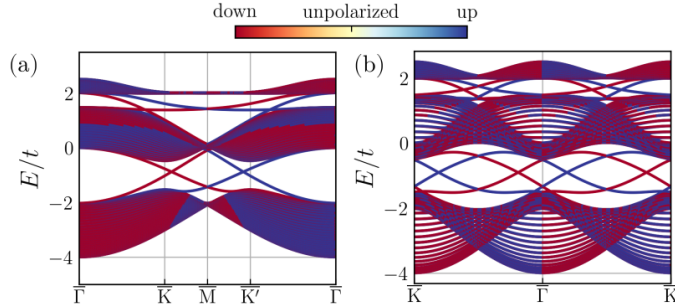


FIG. SF1. Slab kagome bands in the QSH phase corresponding to Fig. 3 in the main text, shown for two different terminations: (a) armchair-flat and (b) zigzag-cove. The color scale represents the spin polarization of the bands. Parameters are $\mu/t = 0$, $\lambda_{KM}/t = 0.15$, and $t = 1$.

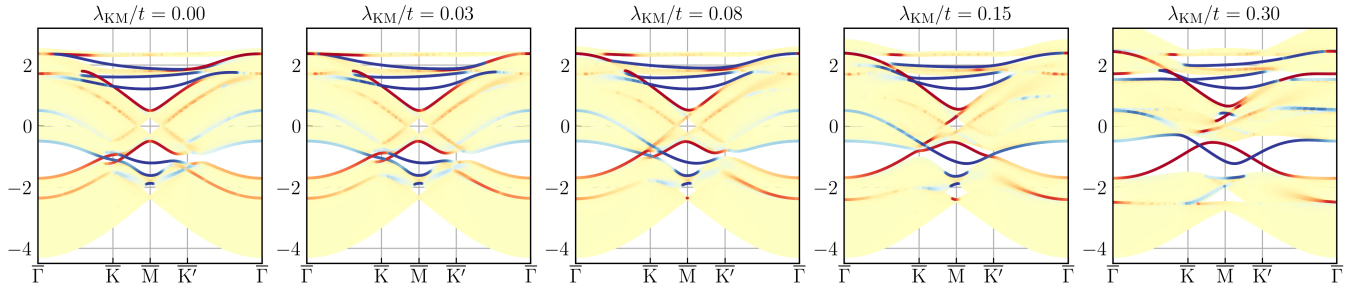


FIG. SF2. Evolution of slab kagome bands with non-coplanar magnetic order [see Fig. 7 in the main text] with increasing Kane–Mele coupling λ_{KM}/t . Color indicates expectation of the position operator. Parameters are $\mu/t = 0$, $J/t = 0.5$, and $t = 1$.